Current Biology, Volume *33*

Supplemental Information

Optogenetics reveals paradoxical network stabilizations in hippocampal CA1 and CA3

Laurel Watkins de Jong, Mohammadreza Mohagheghi Nejad, Euisik Yoon, Sen Cheng, and Kamran Diba

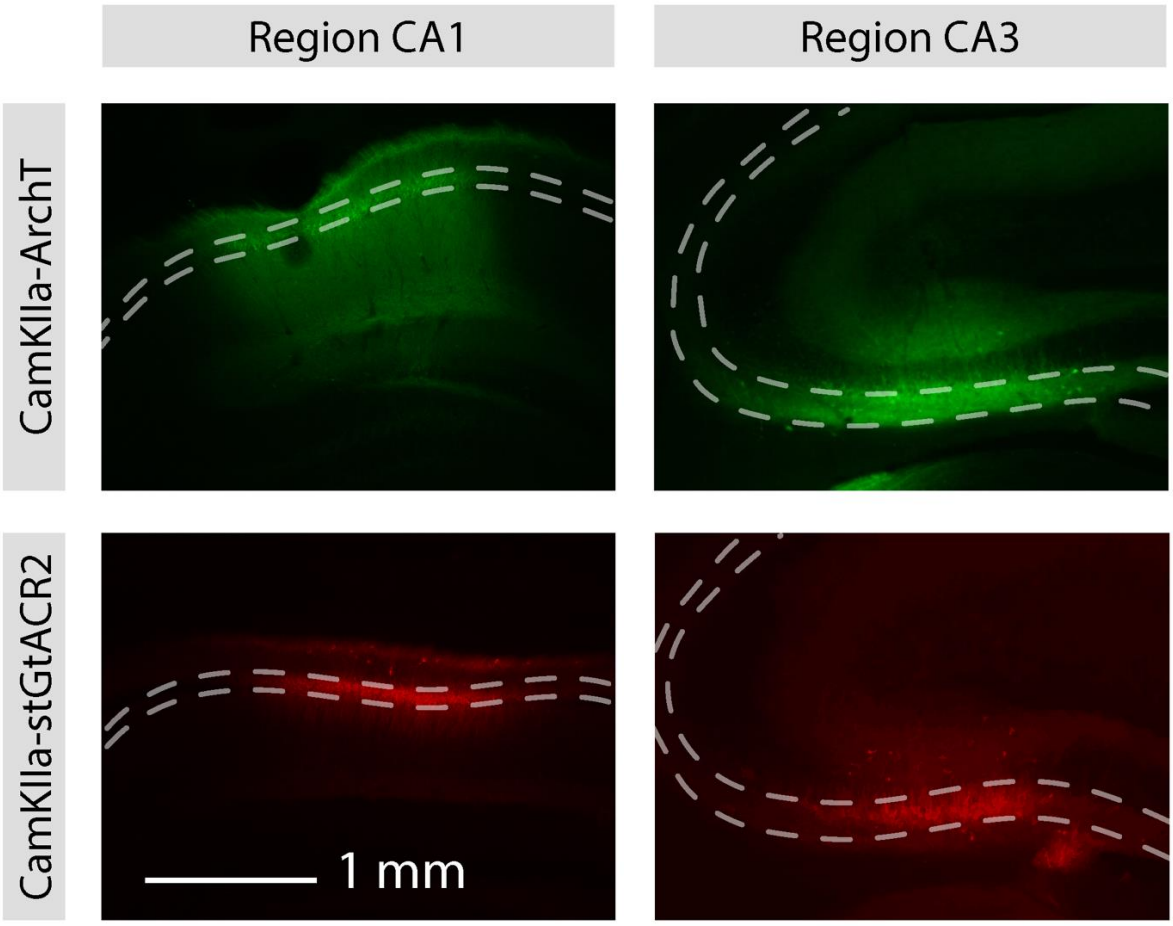

Figure S1: Viral expression in CA1 and CA3. Related to STAR Methods.
Sample expression of AAV2-CamKIIα-ArchT-GFP (top) and AAV1-CamKIIα-stGtACR2-fusionRed (bottom) was confirmed posthoc in rat hippocampal subregions CA1 (left) and CA3 (right). The pyramidal cell layer is contoured with dashed white lines to enhance visibility.

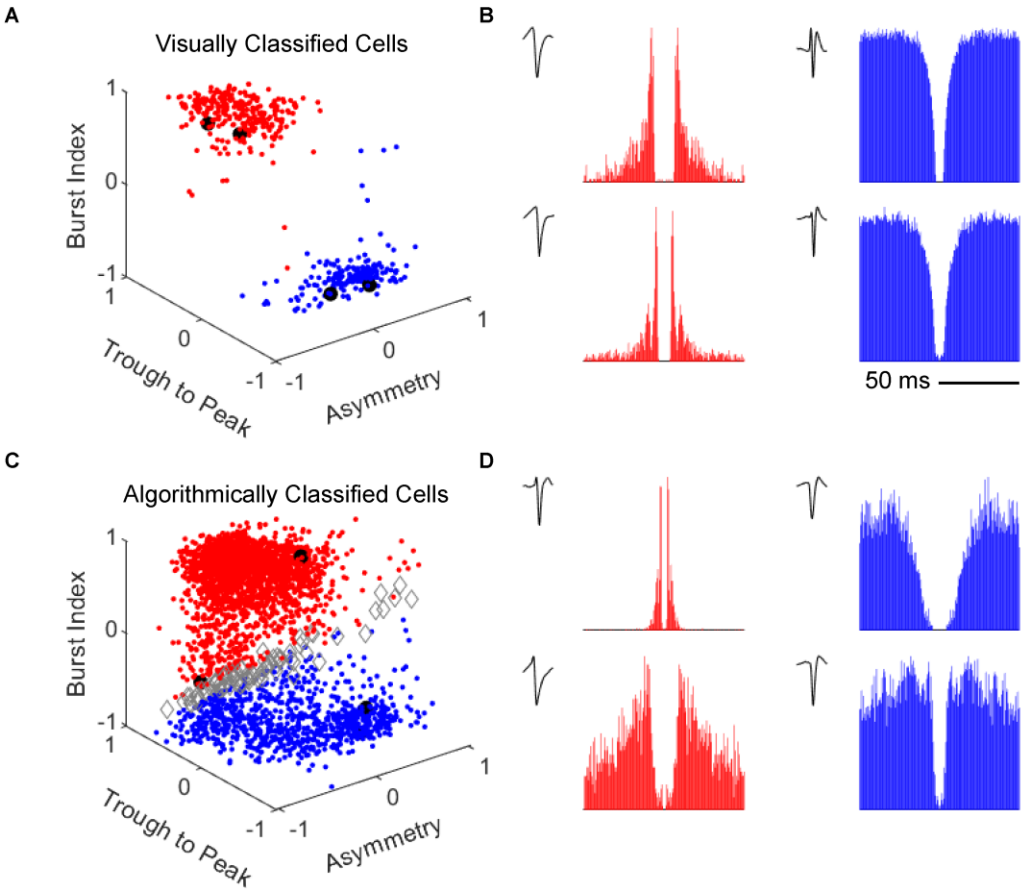

Figure S2: Cell classification with a quadratic classifier. Related to STAR Methods. A) Scatterplot of spiking and waveshape features (left) of visually classified cells (pyramidal: red, interneuron: blue). The recording channel with the largest spike amplitude was chosen for waveshape classification. **B)** Examples of autocorrelograms and waveshapes of two visually classified pyramidal cells (left, red) and two visually classified interneurons (right, blue). **C)** Classification of all cells performed using quadratic discriminant analysis with the visually classified neurons as the training set. Cells with posterior probability between 0.1 and 0.9 (grey) were excluded from analysis. **D)** Examples of autocorrelograms and waveshapes of two pyramidal cells (left, red) and two interneurons (right, blue) identified by the automated classifier.

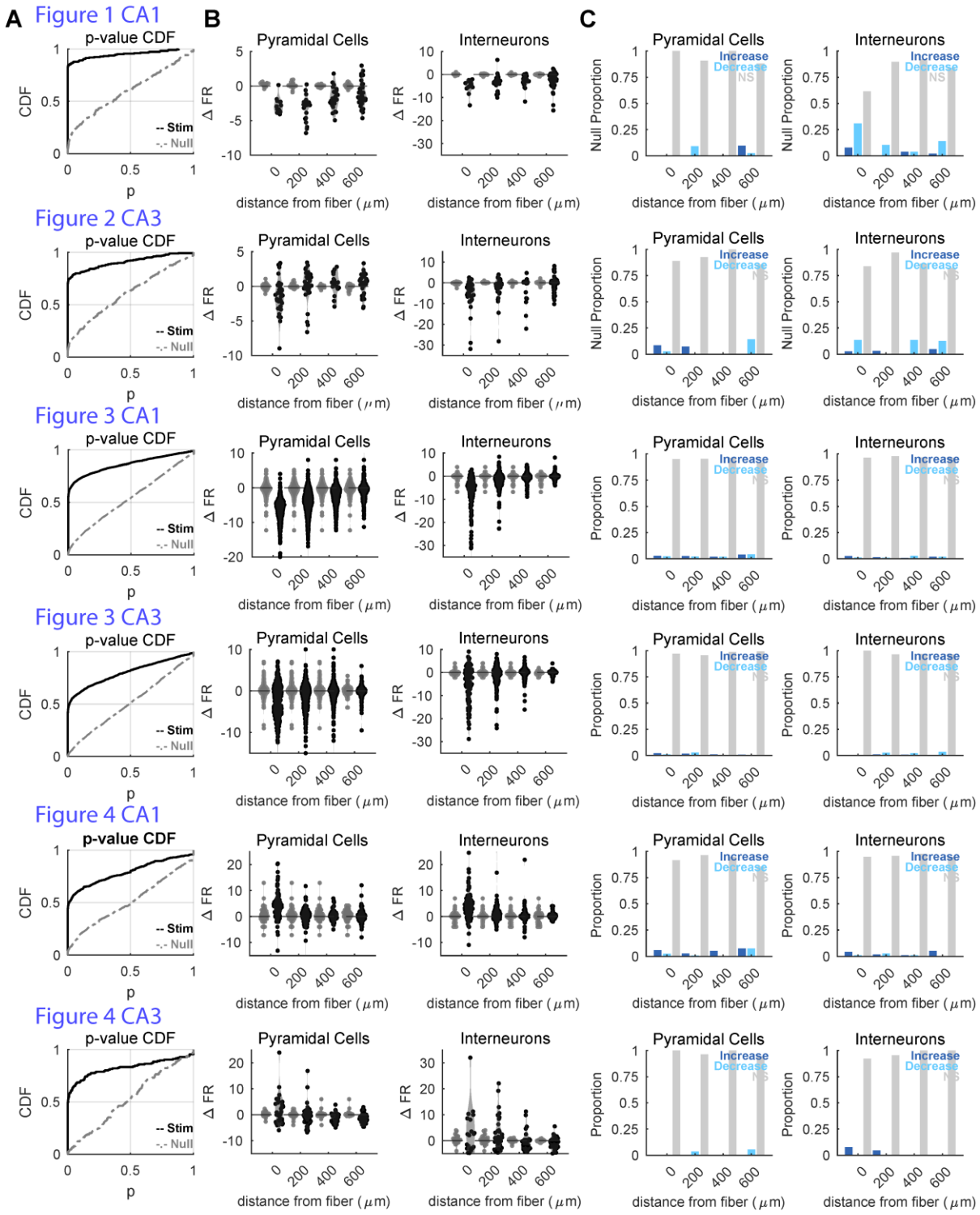

Figure S3. Comparisons with baseline null periods. Related to Figures 1-4. Each row displays results corresponding to the specified CA region and figure in the main manuscript. As described in the STAR Methods, we assessed significance of increases and decreases in firing rates for each recorded neuron in two adjoining windows both from the baseline period, equal in size to the photoillumination

window. These allowed us to assess the likelihood of observing apparently significant changes (at α = 0.01) by chance alone. From left to right, each column of panels depicts the following. **A)** The cumulative distribution function of p-values obtained during photoillumination ('Stim') versus in null ('Null') periods. **B)** The change in firing rates observed by comparing the null periods (gray) compared to photoillumination versus baseline (black) for pyramidal cells (left) and interneurons (right). Note the typically higher variances generated by photoillumination in the data compared to the null periods. F-tests comparing these variances are provided in **Table S3**. **C)** The proportions of null baseline false positives at each the distances of recording electrode relative to the photoillumination site for pyramidal cells (left) and interneurons (right). Fisher's exact tests comparisons of these proportions compared to those in the data are provided in **Table S2**.

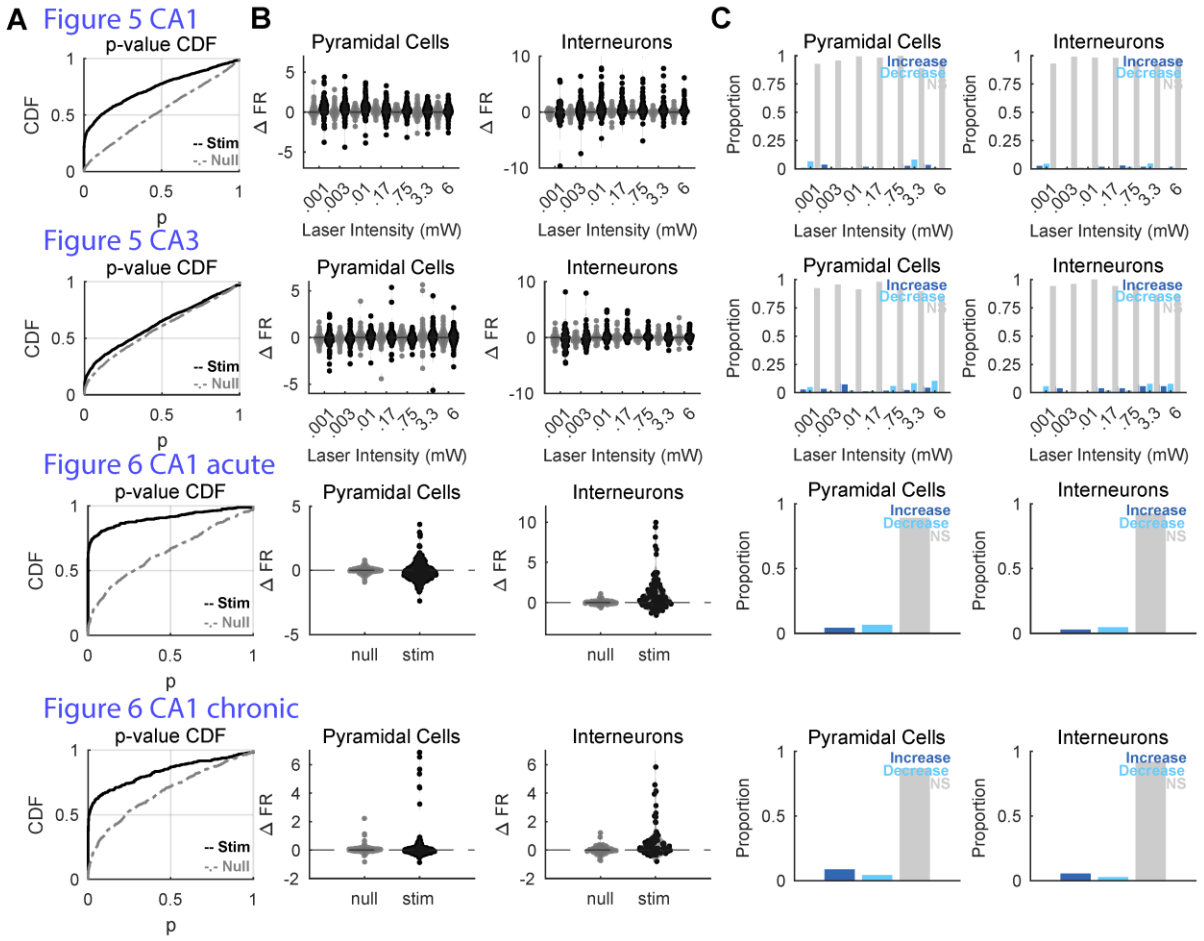

Figure S4. Comparisons with baseline null periods. Related to Figures 5 & 6. Similar to Figure S3. From left to right, each column of panels depicts the following. **A)** The cumulative distribution function of p-values obtained during photoillumination ('Stim') versus in null ('Null') periods. **B)** The change in firing rates observed by comparing the null periods (gray) compared to photoillumination versus baseline (black) for pyramidal cells (left) and interneurons (right). Note the generally higher variances generated by photoillumination in the data compared to the null periods. F-tests comparing these variances are provided in **Table S3**. **C)** The proportions of null baseline false positives at each of the intensity levels in the first two rows, or at all sites combined for the bottom two rows, relative to the photoillumination site for pyramidal cells (left) and interneurons (right). Fisher's exact tests comparisons of these proportions compared to those in the data are provided in **Table S2**.

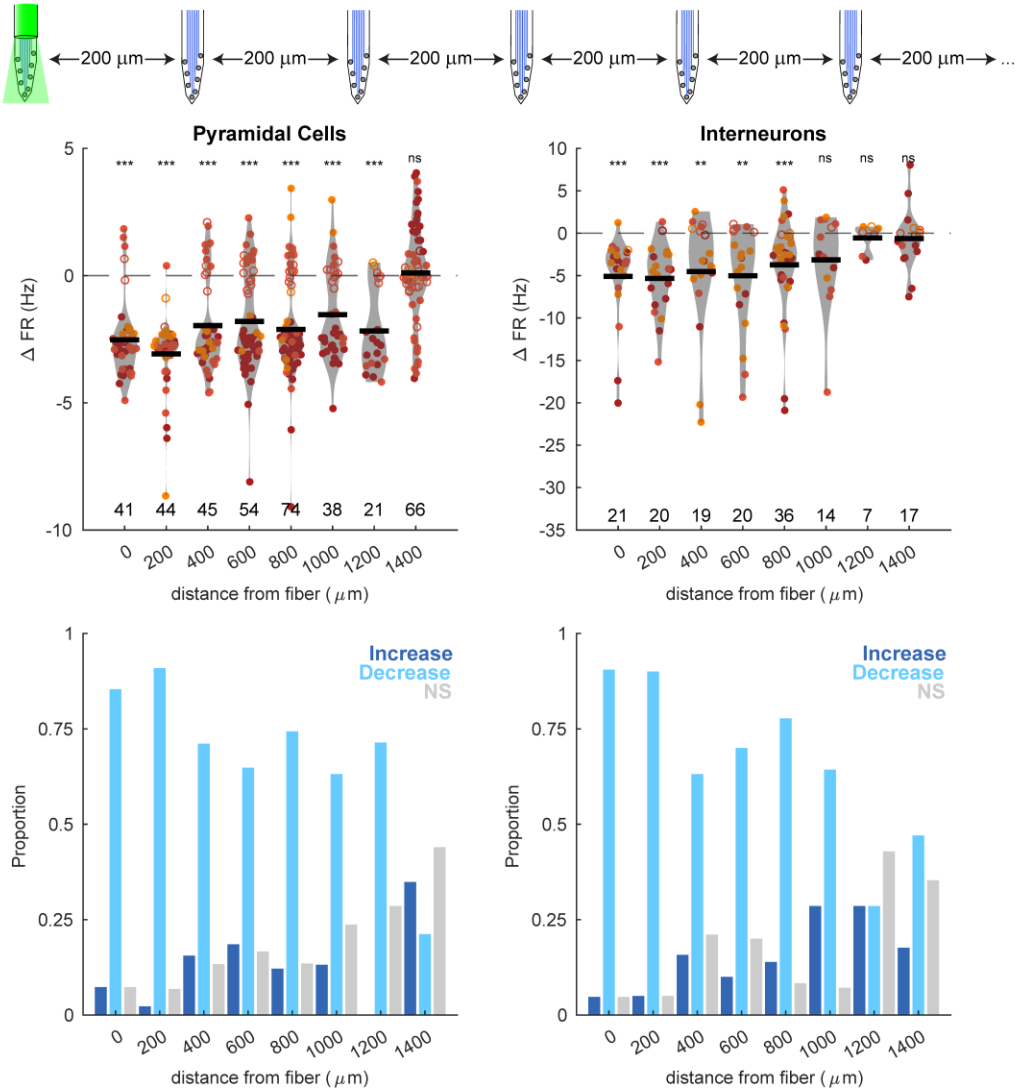

Figure S5: Local and off-target effects of photoinhibition in CA3 with CamKIIα-stGtACR2. Related to Figures 2 and 3. Optrode responses recorded in neurons of animals infused with CamKIIα-stGTACR2 in CA3. Pooled population firing rate responses (top) and proportion plots (bottom) for pyramidal cells (left) and interneurons (right) as a function of distance from the optic fiber. Individual cells overlaid on the population violin plots are colored according to animal, with the black vertical line providing the group mean. Filled circles identify significantly modulated cells (binomial test, $\alpha = 0.01$). Numbers at the bottom of each panel provide the number of cells in each condition. We used an 8-shank silicon probe for these experiments, which provided a larger spatial span for the recordings. Consistent with observations made using CamKIIα-ArchT vectors, in these experiments a large proportion of cells showed a significant change in spiking activity during photo illumination, with some decreasing firing, as expected from photoinhibition, but many others instead increasing in response to light. We note however, particularly strong bimodality in the pyramidal cell responses, similar to those we observed in µLED experiments shown in **Figure 3D** *: $p < .01$, **: $p < .001$, ***: $p < .0001$, paired t-test.

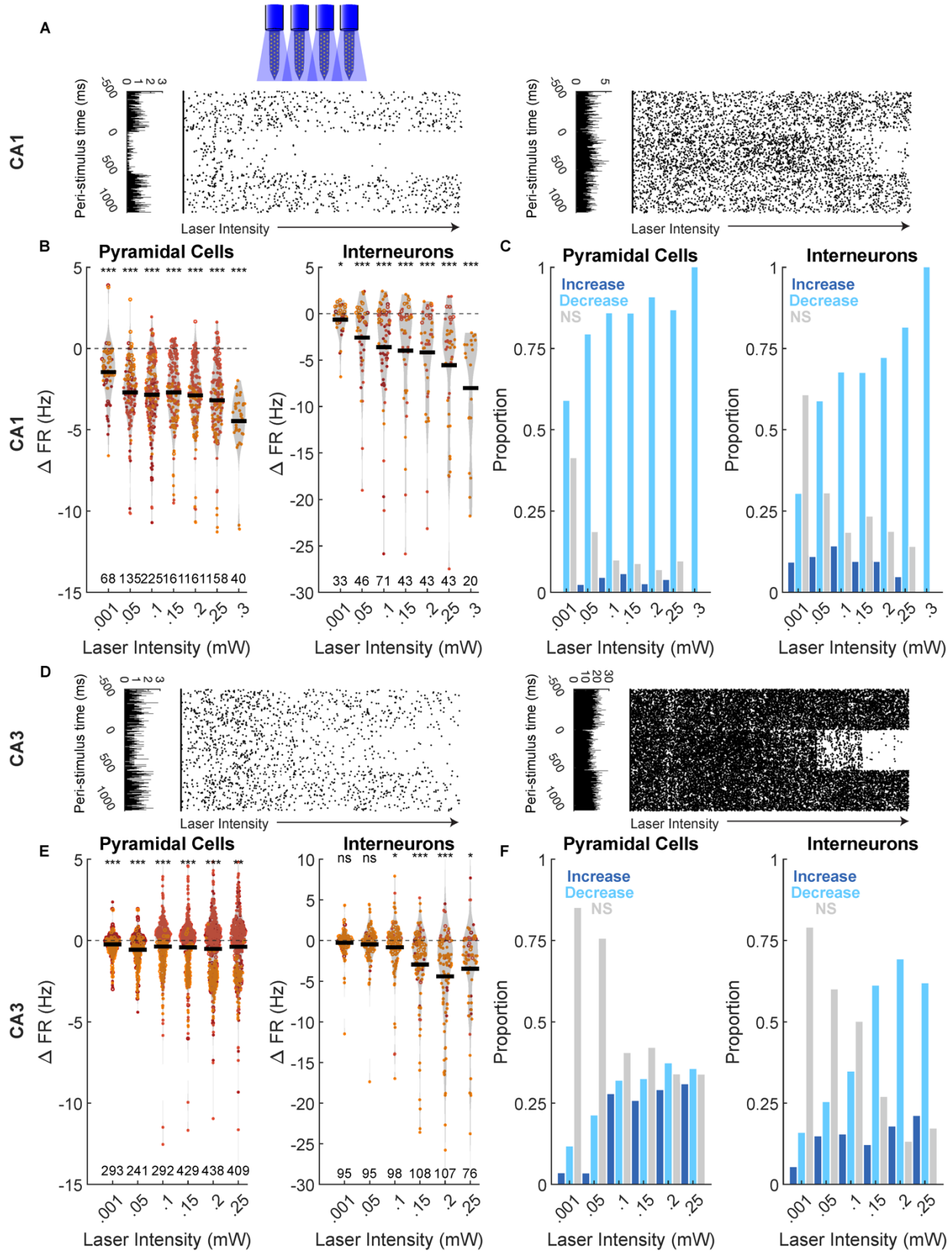

Figure S6: Responses to large-scale photoinhibition of neurons in CA1 and CA3. Related to Figure 5. Neuronal responses to broad multi-fiber photoinhibition in rats expressing CamKIIα-stGtACR2 in CA1 and CA3. **A)** Example raster responses of a pyramidal cell (left) and an interneuron (right) in CA1 across

trials with varying intensities of illumination per fiber from a custom 4-fiber “Masminidis” optrode. The pooled peri-event histograms are provided at the left of the rasters. **B)** Population firing rate changes and **C)** proportion plots for CA1 pyramidal cells (left) and interneurons (right) as a function of laser intensity. Individual cells overlaid on the population violin plots are colored according to animal, with the black vertical line providing the group mean. Filled circles identify significantly modulated cells (binomial test, α = 0.01). Numbers at the bottom of each panel provide the number of cells in each condition. Pyramidal cell firing rates generally decreased with photo-inhibition, while interneurons showed a more bimodal response particularly at low and intermediate light intensities. **D)** Similar to **A,** but for an example pyramidal cell (left) and interneuron (right) in CA3 as light intensity was increased from <0.001 mW to 0.25 mW per fiber. **E)** Population firing rate changes and **F)** proportion plots for CA3 pyramidal cells (left) and interneurons (right) as a function of laser intensity. Pyramidal cell and interneuron responses in these experiments were bimodal, with both increased and decreased firing responses evident at most intensity levels. *: $p < .01$, **: $p < .001$, ***: $p < .0001$, paired t-test.

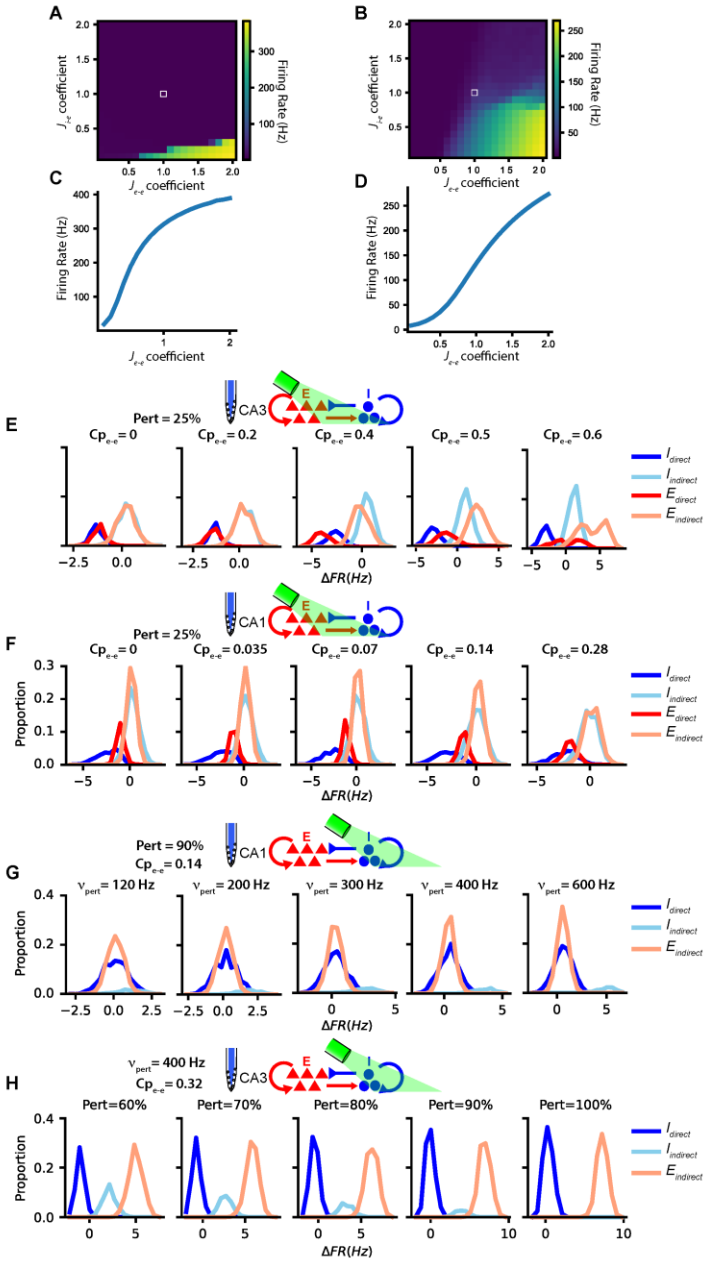

Figure S7: CA1 and CA3 network model parameters and simulations. Related to Figure 7. The average firing rates in the excitatory subpopulation in CA1 (**A)** and CA3 (**B)**, under different parameters for recurrent excitatory and inhibitory conductances. Network dynamics are determined by an interplay between excitation and inhibition. Here, we scaled the excitatory and inhibitory conductances in the model each by a scaling coefficient. When the excitatory conductance, $J_{e\text{-}e}$, is too strong, the networks tend towards the maximum firing rate that the spiking dynamics allow (indicated by the yellow color on the scale bar). In this regime, no information processing is possible in the network. Hence, we chose model parameters (coefficients = 1, white squares) to ensure that both CA1 and CA3 operate in stable regimes. Under the chosen settings for CA1 (**C)** and CA3 (**D)**, removal of inhibition results in excessively high firing and instability at the values of the excitatory conductances used, confirming that these networks are operating in the inhibition stabilized regime. We simulated photoinhibition of **E)** CA3 and **F)** CA1, under different settings of $Cp_{e\text{-}e}$, the connection probability between excitatory (E) cells. Here, we set the % of directly photoinhibited neurons (both E and I) to 25%. As the connection probability was increased, we observed increased firing in a greater number of E and I cells that were not directly perturbed. This effect

appeared stronger in CA3 which was modeled with higher connection probabilities. Interestingly, at the higher setting of $Cp_{e\text{-}e}$= 0.6 for CA3 in the rightmost panel of (A), note the increased firing even in a subset of directly photoinhibited E cells, reflecting the spread of excitation. In panel **G)** we simulated CA1 with $Cp_{e\text{-}e}$= 0.14 and varied the intensity of the photoinhibition (ν_{pert}) to Pert = 90% of the I cells, to simulate experiments depicted in **Figure 5A-C**. The paradoxical increase in directly perturbed I cells becomes evident at higher intensities (rightmost panels). In panel **H)** we simulated CA3 with $Cp_{e\text{-}e}$= 0.32 (ν_{pert} = 400 Hz) and varied the percentage of directly perturbed interneurons. We note that the paradoxical effect in directly perturbed I cells is only apparent at highest values of the perturbation percentage. Compared to simulations for CA1 in panel (G), $E_{indirect}$ firing increases are more apparent in CA3, reflecting the higher e-e connection probability in CA3, but the I_{direct} firing increases are more readily apparent in CA1, likely due to the higher e-i probability in CA1.

Figure	Animal ID	# of Sessions	Virus Location (Hemisphere)	Recording Location	# of Units	Recording Type	Probe Design	Virus Type
1	EO	2	CA1(R)/CA3(L)	CA1	59	Optrode	Neuralynx A4x16	AAV2-CamKIIα-ARCHT-GFP
1	EP	2	CA1(R)/CA3(L)	CA1	117	Optrode	Neuralynx A4x16	AAV2-CamKIIα-ARCHT-GFP
1	EQ	2	CA1(R)/CA3(L)	CA1	55	Optrode	Neuralynx A4x16	AAV2-CamKIIα-ARCHT-GFP
2	DD	1	CA3 (bilateral)	CA3	25	Optrode	Neuralynx Buz32	AAV2-CamKIIα-ARCHT-GFP
2	DG	2	CA3 (bilateral)	CA3	61	Optrode	Neuralynx Buz32	AAV2-CamKIIα-ARCHT-GFP
2	DM	1	CA3 (bilateral)	CA3	21	Optrode	Neuralynx Buz32	AAV2-CamKIIα-ARCHT-GFP
2	DN	2	CA3 (bilateral)	CA3	59	Optrode	Neuralynx Buz32	AAV2-CamKIIα-ARCHT-GFP
2	EO	4	CA1(R)/CA3(L)	CA3	127	Optrode	Neuralynx A4x16	AAV2-CamKIIα-ARCHT-GFP
2	EP	1	CA1(R)/CA3(L)	CA3	41	Optrode	Neuralynx A4x16	AAV2-CamKIIα-ARCHT-GFP
2	EQ	1	CA1(R)/CA3(L)	CA3	8	Optrode	Neuralynx A4x16	AAV2-CamKIIα-ARCHT-GFP
3	FK	2	CA1(R)/CA3(L)	CA1	97	Opto-electrode	NeuroLight µLED	AAV1-CamKIIα-stGtACR2-fusionRed
3	FL	2	CA1(R)/CA3(L)	CA1	166	Opto-electrode	NeuroLight µLED	AAV1-CamKIIα-stGtACR2-fusionRed
3	FM	3	CA1(R)/CA3(L)	CA1	150	Opto-electrode	NeuroLight µLED	AAV1-CamKIIα-stGtACR2-fusionRed
3	FK	2	CA1(R)/CA3(L)	CA3	47	Opto-electrode	NeuroLight µLED	AAV1-CamKIIα-stGtACR2-fusionRed
3	FL	1	CA1(R)/CA3(L)	CA3	9	Opto-electrode	NeuroLight µLED	AAV1-CamKIIα-stGtACR2-fusionRed
3	FM	4	CA1(R)/CA3(L)	CA3	183	Opto-electrode	NeuroLight µLED	AAV1-CamKIIα-stGtACR2-fusionRed
4	EG	4	CA1(R)/CA3(L)	CA1	88	Opto-electrode	NeuroLight µLED	AAV5-hSyn-oCHIEF-tdTomato
4	EH	1	CA1(R)/CA3(L)	CA1	36	Opto-electrode	NeuroLight µLED	AAV5-hSyn-oCHIEF-tdTomato
4	R3	1	CA1(R)/CA3(L)	CA1	27	Opto-electrode	NeuroLight µLED	AAV5-hSyn-oCHIEF-tdTomato
4	R4	2	CA1(R)/CA3(L)	CA1	46	Opto-electrode	NeuroLight µLED	AAV5-hSyn-oCHIEF-tdTomato
4	R3	2	CA1(R)/CA3(L)	CA3	38	Opto-electrode	NeuroLight µLED	AAV5-hSyn-oCHIEF-tdTomato
4	R4	3	CA1(R)/CA3(L)	CA3	37	Opto-electrode	NeuroLight µLED	AAV5-hSyn-oCHIEF-tdTomato
4	ED	2	CA1(R)/CA3(L)	CA3	14	Opto-electrode	NeuroLight µLED	AAV5-hSyn-oCHIEF-tdTomato
5	FR	2	CA1(R)/CA3(L)	CA1	140	Optrode	Masmanidis 128K	AAV1-SIO-stGtACR2-fusionRed
5	FS	2	CA1(R)/CA3(L)	CA1	86	Optrode	Masmanidis 128K	AAV1-SIO-stGtACR2-fusionRed
5	FT	1	CA1(R)/CA3(L)	CA1	38	Optrode	Masmanidis 128K	AAV1-SIO-stGtACR2-fusionRed
5	FR	2	CA1(R)/CA3(L)	CA3	81	Optrode	Masmanidis 128K	AAV1-SIO-stGtACR2-fusionRed

5	FS	2	CA1(R)/CA3(L)	CA3	86	Optrode	Masmanidis 128K	AAV1-SIO-stGtACR2-fusionRed
5	FT	1	CA1(R)/CA3(L)	CA3	80	Optrode	Masmanidis 128K	AAV1-SIO-stGtACR2-fusionRed
6	DD	2	CA3 (bilateral)	CA1	66	Fibers + electrodes	Neuralynx Buz64	AAV2-CamKIIα-ARCHT-GFP
6	DF	2	CA3 (bilateral)	CA1	48	Fibers + electrodes	Neuralynx Buz64	AAV2-CamKIIα-ARCHT-GFP
6	DG	2	CA3 (bilateral)	CA1	105	Fibers + electrodes	Neuralynx Buz64	AAV2-CamKIIα-ARCHT-GFP
6	DH	2	CA3 (bilateral)	CA1	225	Fibers + electrodes	Neuralynx Buz64	AAV2-CamKIIα-ARCHT-GFP
6	DS*	2	CA3 (bilateral)	CA1	119	Fibers + electrodes	Neuralynx Buz32	AAV2-CamKIIα-ARCHT-GFP
6	DX*	2	CA3 (bilateral)	CA1	138	Fibers + electrodes	Neuralynx Buz32	AAV2-CamKIIα-ARCHT-GFP
6	DZ*	2	CA3 (bilateral)	CA1	19	Fibers + electrodes	Cambridge P-64	AAV2-CamKIIα-ARCHT-GFP
6	EA*	2	CA3 (bilateral)	CA1	55	Fibers + electrodes	Cambridge P-64	AAV2-CamKIIα-ARCHT-GFP
S3	FN	2	CA1(R)/CA3(L)	CA1	114	Optrode	Masmanidis 128K	AAV1-CamKIIα-stGtACR2-fusionRed
S3	FP	2	CA1(R)/CA3(L)	CA1	145	Optrode	Masmanidis 128K	AAV1-CamKIIα-stGtACR2-fusionRed
S3	FQ	2	CA1(R)/CA3(L)	CA1	60	Optrode	Masmanidis 128K	AAV1-CamKIIα-stGtACR2-fusionRed
S3	FN	2	CA1(R)/CA3(L)	CA3	171	Optrode	Masmanidis 128K	AAV1-CamKIIα-stGtACR2-fusionRed
S3	FP	2	CA1(R)/CA3(L)	CA3	206	Optrode	Masmanidis 128K	AAV1-CamKIIα-stGtACR2-fusionRed
S3	FQ	3	CA1(R)/CA3(L)	CA3	188	Optrode	Masmanidis 128K	AAV1-CamKIIα-stGtACR2-fusionRed
S4	FC	2	CA3 (bilateral)	CA3	241	Optrode	Neuralynx Buz64	AAV1-CamKIIα-stGtACR2-fusionRed
S4	FD	2	CA3 (bilateral)	CA3	211	Optrode	Neuralynx Buz64	AAV1-CamKIIα-stGtACR2-fusionRed
S4	FE	2	CA3 (bilateral)	CA3	101	Optrode	Neuralynx Buz64	AAV1-CamKIIα-stGtACR2-fusionRed

Table S1. Table of experimental details pertaining to Figures 1-6. Related to STAR methods.

Figure	Cell Type	Proportion Comparison p-values (Fisher's Exact Test)								
		0 μm	200 μm	400 μm	600 μm	Contrast across distance	Null contrast across distance			
1C	pyr	1.00	1.00	1.00	0.52	0.06108	0.2416			
	int	1.00	1.00	1.00	0.20	0.3152	0.3862			
2C	pyr	0.48	**1.12E-04**	**3.09E-03**	**1.28E-07**	**5.57E-03**	0.2515			
	int	0.20	0.05	0.11	**1.28E-04**	0.1957	0.9249			
3C	pyr	0.28	0.14	**0.0249**	0.15	**8.24E-04**	0.2576			
	int	0.54	**0.001119**	**3.74E-04**	0.10	0.17	0.3869			
3E	pyr	**4.31E-12**	**2.2E-16**	**1.37E-10**	**2.54E-03**	**0.04519**	0.6173			
	int	**8.81E-06**	**1.16E-09**	**1.82E-04**	0.12	0.09	0.8505			
4C	pyr	0.06	**7.68E-07**	**8.98E-03**	0.4316	0.09	0.1154			
	int	**0.004044**	0.08	0.12	0.4966	0.15	0.5855			
4E	pyr	0.11	1.00	**0.0485**	**0.04075**	0.08	0.5678			
	int	0.10	1.00	0.48	1	0.25	1			
		0.001 mW	0.003 mW	0.01 mW	0.17 mW	0.75 mW	3.3 mW	6 mW	Contrast across intensities	Null constrast across intensities
5C	pyr	**4.50E-05**	0.1311	**2.51E-06**	**6.79E-06**	**6.06E-16**	**5.66E-14**	**2.19E-08**	**5.00E-07**	0.1674
	int	**8.84E-04**	**1.59E-07**	**1.81E-12**	**1.15E-08**	**1.63E-12**	**2.62E-09**	**1.06E-04**	**2.26E-04**	0.5233
5F	pyr	0.1341	**1.53E-03**	**6.29E-03**	0.0615	0.05273	0.111	1	**7.28E-04**	**0.04004**
	int	**0.02683**	0.6781	**0.02683**	0.4367	**0.02814**	0.07211	0.3189	0.5047	0.3779
		CA1 response wrt CA3								
6A	pyr	**2.36E-13**								
	int	**2.20E-16**								
6B	pyr	**9.50E-06**								
	int	**2.60E-10**								

Table S2. Statistical proportion comparisons with baseline nulls. Related to Figures 1-6.

Figure	Cell Type	ΔFR (F-test)											
		0 μm			200 μm			400 μm			600 μm		
		df	Fstat	p-value	df	Fstat	p-value	df	Fstat	p-value	df	Fstat	p-value
1B	pyr	13	12.64	**5.13E-05**	21	15.96	**2.63E-08**	24	80.78	**2.66E-17**	41	41.74	**6.47E-23**
	int	12	43.91	**1.02E-07**	28	100.32	**2.95E-21**	25	61.14	**1.71E-16**	49	128.29	**9.89E-39**
2B	pyr	35	43.16	**5.23E-23**	40	47.86	**1.57E-23**	18	56.11	**6.62E-12**	34	16.11	**1.01E-12**
	int	36	154.7	**2.82E-30**	32	390.62	**1.89E-33**	21	98.6	**3.44E-16**	62	33.82	**3.16E-31**
3B	pyr	684	3.37	**2.72E-52**	913	3.19	**8.35E-64**	662	2.23	**5.11E-24**	398	1.87	**6.18E-10**
	int	156	17.46	**5.01E-51**	213	4.81	**4.35E-26**	146	1.74	**0.001**	102	0.702	0.075
3D	pyr	339	4.98	**6.65E-45**	547	3.37	**3.98E-42**	334	2.73	**9.43E-20**	125	1.93	**0.0002**
	int	130	45.77	**7.56E-73**	201	15.33	**1.15E-67**	135	7.74	**8.72E-30**	54	2.46	**0.0009**
4B	pyr	104	3.42	**1.25E-09**	103	1.89	**0.001**	61	0.67	0.11	68	1.16	0.52
	int	119	30.22	**5.55E-53**	114	12.38	**2.31E-33**	92	2.47	**2.36E-05**	74	2.67	**1.80E-05**
4D	pyr	23	29	**1.02E-11**	26	8.95	**2.42E-07**	21	1.27	0.59	17	1.07	0.89
	int	14	20.08	**1.43E-06**	22	14.03	**7.83E-08**	16	23.23	**1.92E-07**	9	17.59	**0.0002**
		0.001 mW			0.003 mW			0.01 mW			0.17 mW		
		df	Fstat	p-value	df	Fstat	p-value	df	Fstat	p-value	df	Fstat	p-value
5B	pyr	138	1.06	0.7	138	1.25	0.18	138	2.49	**1.30E-07**	112	3.72	**1.99E-11**
	int	112	3.16	**3.24E-09**	115	8.98	**7.23E-27**	114	14.04	**4.95E-36**	103	13.11	**4.38E-32**
5E	pyr	183	1.54	**0.003**	183	1.31	0.06	182	0.86	0.31	183	1.68	**0.0004**
	int	51	1.24	0.45	51	1.96	**0.01**	51	3.67	**7.64E-06**	51	2.67	**0.0006**
		0.75 mW			3.3 mW			6 mW					
		df	Fstat	p-value	df	Fstat	p-value	df	Fstat	p-value			
5B	pyr	112	4.96	**7.70E-16**	110	2.78	**1.67E-07**	86	2.95	**9.77E-07**			
	int	105	48.18	**1.69E-59**	105	24.12	**1.27E-44**	52	50.51	**9.56E-31**			
5E	pyr	181	0.89	0.43	183	2.1	**7.33E-07**	182	2.44	**2.26E-09**			
	int	51	3.13	**7.84E-05**	51	4.76	**1.17E-07**	51	5.74	**4.33E-09**			
		All											
		df	Fstat	p-value									
6A	pyr	302	11.94	**3.14E-84**									
	int	104	66.4	**6.08E-66**									
6B	pyr	251	34.76	**6.15E-123**									
	int	73		**1.02E-35**									

Table S3. Statistical comparisons of variance with baseline nulls. Related to Figures 1-6.

Studies	Findings most relevant to this study	Comments
Tsodyks, et al. J Neurosci (1997) [S1]	Strong recurrent excitatory connectivity with inhibitory stabilization in CA1 can account for phase coupling between excitatory and inhibitory neurons during theta oscillations.	This prediction is directly tested in our experiments shown in Figure 5a-c.
Litwin-Kumar, et al. J Neurophysiol (2016) [S2] Mahrach et al., eLife (2020) [S3]	Networks composed of multiple inhibitory subtypes that are not inhibitory stabilized (non-ISNs) can produce apparently paradoxical effects when one subtype of inhibitory neuron is perturbed.	These observations suggest that paradoxical effects observed in Figures 1-4 in our study could conceivably be produced without strong recurrent excitation.
Sadeh, et al. J Neurosci (2017) [S4]	Even with multiple inhibitory subtypes, inhibitory stabilization can be revealed by perturbing a large population of interneurons simultaneously.	This study directly motivated our Figure 5 experiments with GAD-cre rats to broadly target inhibitory neurons.
Moore, et al. Neuron (2018) [S5]	Suppression of PV+ interneurons in networks with strong feedforward excitation can produce paradoxical firing increases in downstream PV+ interneurons	We observe a similar effect in CA1 following CA3 photoinhibition, as shown in Figure 6 and in our model (Figure 7).
This paper, Watkins de Jong et al. (2023)	1) Inhibitory stabilized network models can account for off-target responses in both excitatory and inhibitory hippocampal neurons following optogenetic perturbations. 2) Excitatory inputs from CA3 to excitatory and inhibitory cells in CA1 produce paradoxical firing increases in CA1 interneurons following CA3 photoinhibition.	We model both CA1 and CA3 as ISNs. We implement a higher connection probability in CA3 but stronger connection strength in CA1. These differences affect the quality of off-target effects, similar to the data (see Figures 7 and S7 for further details).

Table S4. Summary of modeling results most relevant to the presented work. Related to Figure 7 and Discussion.

S1. Tsodyks, M.V., Skaggs, W.E., Sejnowski, T.J., and McNaughton, B.L. (1997). Paradoxical effects of external modulation of inhibitory interneurons. J Neurosci *17*, 4382-4388.

S2. Litwin-Kumar, A., Rosenbaum, R., and Doiron, B. (2016). Inhibitory stabilization and visual coding in cortical circuits with multiple interneuron subtypes. J Neurophysiol *115*, 1399-1409. 10.1152/jn.00732.2015.

S3. Mahrach, A., Chen, G., Li, N., van Vreeswijk, C., and Hansel, D. (2020). Mechanisms underlying the response of mouse cortical networks to optogenetic manipulation. eLife *9*. 10.7554/eLife.49967.

S4. Sadeh, S., Silver, R.A., Mrsic-Flogel, T.D., and Muir, D.R. (2017). Assessing the Role of Inhibition in Stabilizing Neocortical Networks Requires Large-Scale Perturbation of the Inhibitory Population. J Neurosci *37*, 12050-12067. 10.1523/JNEUROSCI.0963-17.2017.

S5. Moore, A.K., Weible, A.P., Balmer, T.S., Trussell, L.O., and Wehr, M. (2018). Rapid Rebalancing of Excitation and Inhibition by Cortical Circuitry. Neuron *97*, 1341-1355 e1346. 10.1016/j.neuron.2018.01.045.